Faraday Discussions

Direct Frequency Comb Spectroscopy of HCN to Evaluate Line Lists

Journal:	*Faraday Discussions*
Manuscript ID	FD-ART-01-2023-000019.R1
Article Type:	Paper
Date Submitted by the Author:	13-Feb-2023
Complete List of Authors:	Bailey, D. Michelle; National Institute of Standards and Technology, Material Measurement Laboratory Crump, Eric; National Institute of Standards and Technology, Material Measurement Laboratory; University of Maryland at College Park, Department of Chemistry and Biochemistry Hodges, Joseph; National Institute of Standards and Technology, Material Measurement Laboratory Fleisher, Adam; National Institute of Standards and Technology, Material Measurement Laboratory

ARTICLE

Direct frequency comb spectroscopy of HCN to evaluate line lists

D. Michelle Bailey,[a] Eric M. Crump, [a,b] Joseph T. Hodges [a] and Adam J. Fleisher [*a]

Received 00th January 20xx,
Accepted 00th January 20xx

DOI: 10.1039/x0xx00000x

We report direct frequency comb spectroscopy of the $2\nu_1$ band of $H^{13}CN$ in the short-wave infrared (λ = 1.56 μm) towards experimental validation of molecular line lists that support observatories like JWST. The laboratory measurements aim to test spectral reference data generated from an experimentally accurate potential energy surface (PES) and an *ab initio* dipole moment surface (DMS) calculated from quantum chemistry theory. Benchmarking theory with experiment will improve confidence in new astrophysics and astrochemistry inferred from spectroscopic observations of HCN and HNC. Here we describe our instrumentation and initial results using a cross-dispersed spectrometer with a virtually imaged phased array (VIPA).

Introduction

Hydrogen cyanide (HCN) has been observed in dense interstellar clouds [1], star-forming regions [2], comets [3], the atmosphere of Saturn's moon Titan [4], the atmosphere of Pluto [5] and exoplanetary atmospheres [6,7]. When detected with the hydrogen isocyanide (HNC) isomer, the relative abundances of HCN and HNC and their respective isotopic compositions are used as indicators of local temperature and chemistry [8]. For example, HNC is suggested as a tracer to identify proto-brown dwarfs [9] and as a useful chemical clock for star formation [2]. In thermal environments, the HCN/HNC equilibrium constant becomes an important parameter [10].

In general, observational research into the chemistry or physics of many of these objects and associated phenomena depends upon models that use spectral reference data. Therefore, complete molecular line lists to model extreme environments, generated from theory and benchmarked by low-uncertainty experiments, are broadly required [11].

For HCN and HNC, there are several sources of spectral reference data for modeling astrophysical observations. They include HITRAN [12], GIESA [13] and ExoMol [14]. In 2018, a calculated line-list for HCN and HNC showed improved agreement with experiments [15] and was merged into HITRAN2020 [12]. There, calculated transition intensities for $H^{13}CN$ were in good agreement with the transition intensities measured by dual electro-optic frequency comb spectroscopy [16]. A subsequently larger and more comprehensive update to the experimentally accurate potential energy surface (PES) and *ab initio* dipole moment surface (DMS) for HCN was recently completed and presented as the MOMeNT-90 line list [17] — intended for integration with a future HITRAN update. Importantly, the best theory for the molecular PES and DMS can include both HCN and HNC isomers. Therefore, benchmarking spectral reference data for either species can improve our ability to predict and model spectroscopic observations of both isomers.

Here we report direct frequency comb spectroscopy to benchmark HCN line lists calculated from theory. Specifically, we use a free-running mode-locked laser and a cross-dispersed spectrometer to resolve molecular absorption by rovibrational transitions. Our comb-mode-resolved spectrometer enables precise molecular spectroscopy of the $2\nu_1$ band of $H^{13}CN$ in the short-wave infrared near a wavelength of λ = 1.56 μm. We report on spectrometer performance and compare the HITRAN2020 line list with our experimental results. Progress towards the acquisition of metrology-grade HCN and HNC spectral reference data using direct frequency comb spectroscopy in both the short-wave and mid-wave infrared is discussed.

Experiment

Optical frequency comb laser source

Here we use an optical frequency comb [18,19] to perform direct molecular spectroscopy [20]. Illustrated in **Fig. 1** are both the time-domain and frequency-domain representations of the high resolution and broadband laser source. In this work, we used mode-locked lasers as the frequency comb sources. In the time domain, the optical frequency comb emitted from a laser cavity comprises a series of pulses with a fixed period of $1/f_{rep}$, where f_{rep} is the comb repetition rate. Illustrated in **Fig. 1**, the optical carrier frequency of the light pulses (blue line) and the laser pulse envelope (black dashed line) has a pulse-to-pulse phase shift defined as $\Delta\phi = 2\pi f_0/f_{rep}$, where f_0 is the carrier-envelope-offset frequency.

[a] *Material Measurement Laboratory, National Institute of Standards and Technology, Gaithersburg, MD 20899, USA.*
[b] *Department of Chemistry and Biochemistry, University of Maryland, College Park, MD 20742, USA.*
* Corresponding author E-mail: adam.fleisher@nist.gov

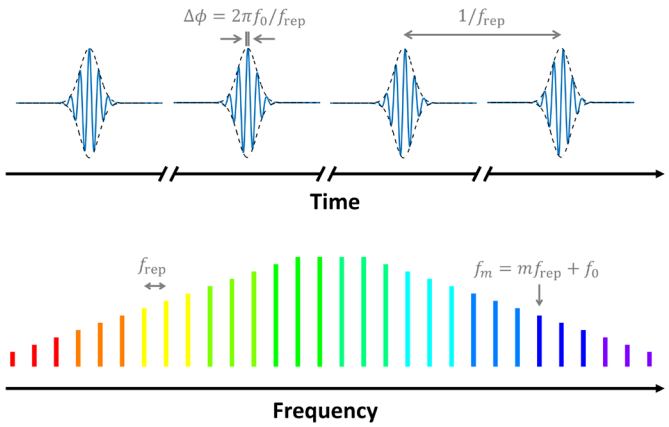

Fig. 1. Illustration of an optical frequency comb. The top panel shows a time-domain representation of a train of laser pulses with an optical carrier frequency (blue line) and pulse envelope (black dashed line). The phase shift between the carrier and envelope is $\Delta\phi = 2\pi f_0/f_{rep}$. The bottom panel shows the corresponding frequency domain spectrum of the train of pulses, revealing individual comb teeth separated by the laser repetition rate f_{rep} and each with unique optical frequencies $f_m = mf_{rep} + f_0$, where m is the tooth index and f_0 is the carrier envelop offset frequency.

The Fourier transform of the train of stable laser pulses yields a series of narrow-linewidth lasers in the frequency domain, each with a unique mode index m. Each tooth has a fixed frequency spacing of f_{rep} and an absolute optical frequency of $f_m = mf_{rep} + f_0$. More details regarding frequency combs and their applications can be found in recent review articles (e.g., [21,22]).

Direct frequency comb spectroscopy

The direct frequency comb spectrometer reported here comprised a mode-locked laser source, repetition-rate-monitoring electronics, fiber-coupled gas sample cell and cross-dispersed spectrometer. An illustration is shown in **Fig. 2**.

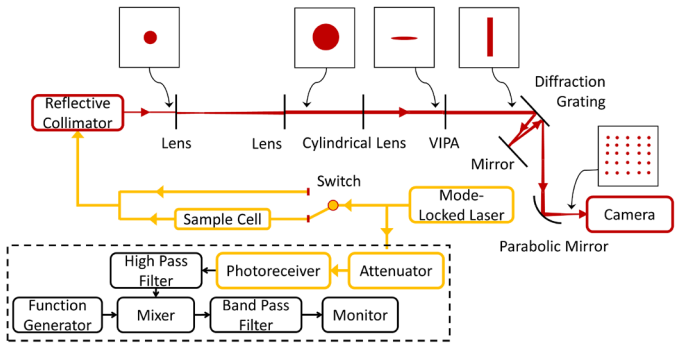

Fig. 2. Direct frequency comb spectrometer. Shown in the block diagram are the mode-locked laser source, gas sample and reference beam paths, sample cell, beam shaping optics and the cross-dispersed spectrometer. Fiber-coupled and free-space laser paths are illustrated with yellow and red arrows, respectively, and electronic signals for comb repetition rate monitoring are illustrated with black arrows. Image insets illustrate how the free-space laser beam profile transforms along its optical path, resulting in comb-mode-resolved images being recorded by the infrared camera. Optical dispersion within the beam profiles is not illustrated.

The frequency comb was a solid-state mode-locked laser (Menhir Photonics; MENHIR-1550) ‡ with repetition rate of f_{rep} = 1.00 GHz. The value of f_{rep} was monitored by measuring the beat frequency $f_{beat} = 3\times(f_{rep}-f_{LO})$, where f_{LO} = 0.986 580 7 GHz. Therefore, f_{beat} ≈ 40 MHz. The carrier envelope offset frequency (f_0) of the mode-locked laser was not stabilized and its value not monitored during measurements. As a result, each spectral acquisition comprises a highly precise grid of relative optical frequencies emitted from the mode-locked laser and defined by f_{rep}, but with an uncertain absolute offset frequency, f_0. We note that the mode-locked laser used here can be self-referenced using an f–$2f$ interferometer, thus creating an absolute frequency comb [23].

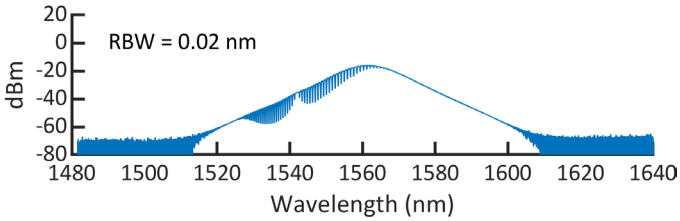

Fig. 3. Optical power spectrum of the mode-locked laser frequency comb after passing through the $H^{13}CN$ multipass gas-sample cell. RBW, resolution bandwidth of the optical spectrum analyzer.

The fiber-coupled output of the frequency comb was connected to a 1×2 fiber optic switch. One arm of the switch output was fiber-coupled to a commercial multipass gas sample cell (Wavelength References; HCN-13-100), whereas the second arm bypassed the gas sample cell and was used as a spectral reference channel. The gas sample cell was also discussed in a prior publication [16] and contained $H^{13}CN$ of molecular purity of >95 % and isotopic purity of 99 % at a pressure of 13.2 kPa ± 0.3 kPa. The absorption path length was L = 79 cm ± 1 cm. The optical power spectrum of the comb after passing through the $H^{13}CN$ sample is shown in **Fig. 3**.

The sample and reference arms were recombined in fiber and the collimated output was sent into free space towards a pair of lenses for beam expansion to a 20 mm collimated beam diameter. The larger-diameter beam was then sent to the spectrometer which ultimately resolved individual frequency comb modes on a two-dimensional detector array.

Cross-dispersed spectrometer and image analysis

The cross-dispersed spectrometer comprised a cylindrical lens, virtually imaged phased array (VIPA) etalon, double-passed ruled diffraction grating, imaging lens and infrared camera. The experimental set-up shares some similarities with several other previously reported comb-mode-resolved spectrometers [24–29].

The cylindrical lens creates a line-focused beam profile at the entrance of the VIPA etalon, as illustrated in the top of **Fig. 2**. The VIPA etalon (Light Machinery; OP-6721-6743-8) is oriented such that the incident beam enters ≈1° off-normal. Transmission of the high-dispersion VIPA is governed by its dispersion law [30] and its characteristics determine several important spectrometer parameters. These include the VIPA etalon linewidth (full-width at half maximum), $\delta\nu_{VIPA}$ = 0.107 GHz; free-spectral-range (FSR), ν_{FSR} = 15 GHz; and finesse, $\mathcal{F}$ = 140.

Dispersion from the VIPA is further separated — or cross-dispersed — using a ruled diffraction grating to create the two-

dimensional image. Rotation of the diffraction grating results in a different portion of the broadband laser source being incident on the camera. Therefore, broadband optical tuning of the spectrometer was achieved by rotating the diffraction grating to a new position.

An example image from the cross-dispersed spectrometer is show in **Fig. 4**. Each gray dot is signal from a unique optical frequency comb tooth convolved with the instrument line shape (ILS) function. The ILS is a combination of the VIPA etalon linewidth and any additional broadening components such as standard single slit transmission broadening found in grating spectrometers. The composite ILS is modeled here by a simple Voigt function fitted for each imaged comb tooth along the vertical VIPA-dispersion direction. An example ILS fit is shown in **Fig. 4** for a representative column of pixels from a typical reference image without molecular absorption.

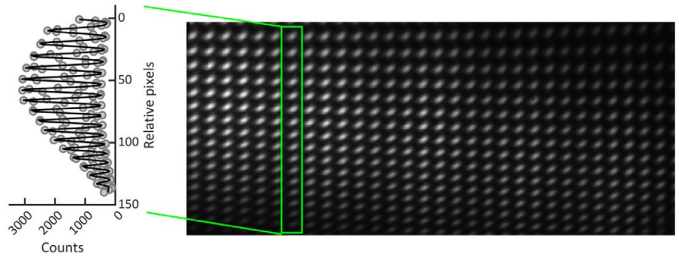

Fig. 4. Cross-dispersed spectrometer reference image with comb-mode resolution. The light gray dots on a field of black background are the resolved comb teeth, each with a unique and precisely known optical frequency. The vertical axis in the image is the VIPA dispersion direction and the horizontal axis is the grating dispersion direction. Counts from a column of pixels comprising one VIPA etalon free-spectral range is highlighted by the green box. On the far-left hand side is a rotated plot of camera counts vs. relative pixel position (gray dots) and the sum of the fitted instrument line shape (ILS) functions (black line).

With ν_{FSR} = 15 GHz and f_{rep} = 1.00 GHz, there are 15 unique optical frequency comb teeth that comprise each column of unique comb teeth in **Fig. 4**. The VIPA orders are spatially separated in the horizontal dimension by the grating, and each image comprises up to 30 VIPA orders. Therefore, our spectrometer covers a bandwidth of 450 GHz at a single grating position, or 15 cm^{-1} in the short-wave infrared near 6410 cm^{-1}. The fitted full-width at half maximum of the composite ILS is nominally 0.44 GHz across the majority of the image, yielding a spectrometer resolving power of $R = \nu/\delta\nu$ = 4.4×10^5.

At an image integration time of 100 µs, we observe several thousand camera counts at the peak of each comb tooth. Here, the spectrometer bandwidth and resolving power are limited by our initial optical alignment and the choice of available imaging and beam shaping optics and can be improved by the inclusion of achromatic lenses and the subsequent reduction of optical aberrations near the edges of the image at the camera focal plane array.

Spectral modeling

To model the experimental transmission spectrum, the cross-dispersed spectrometer ILS function, $G(\tilde{\nu})$, can be convolved with the molecular transmission spectrum simulation as sampled at each comb tooth [31]. This is written in Eq. (1):

$$\mathcal{T}(\tilde{\nu}) = \exp\{-\alpha(\tilde{\nu})L\} \otimes G(\tilde{\nu}). \qquad (1)$$

Above, $\alpha(\tilde{\nu})$ is the absorption coefficient as a function of wavenumber, $\tilde{\nu}$, and L is the sample path length.

Alternatively, the ILS can be effectively deconvolved from the columns in each experimental image (e.g., **Fig. 4**) by the sifting property of a delta function. By assuming that the comb tooth linewidth is negligible compared to the ILS width, the modeled molecular transmission spectrum can be directly compared with the deconvolved comb tooth intensities.

The choice of modeling approach may depend upon the resolution of the cross-dispersed spectrometer compared to the comb mode spacing. Here in the short-wave infrared, with a nominal resolution of 0.4 GHz and a comb mode spacing of f_{rep} = 1.00 GHz, the comb modes may be considered resolved and effective deconvolution pursued.

Analysis of spectral noise limits

Here we present a brief analysis of the anticipated noise limits based on infrared camera manufacturer specifications and observations, optical frequency comb power measurements and estimated spectrometer throughput. We consider the following sources: detector noise, photon shot noise and quantization noise due to finite camera bit depth.

To estimate the influence of detector noise, we converted the camera noise-equivalent temperature difference of NETD = 60 mK to an irradiance noise from a blackbody source at a laboratory temperature of T = 297 K. Here we assume that only photons within the camera wavelength responsivity range of 1.5 µm to 5.1 µm contribute to the noise. To convert the calculated blackbody radiance [32] to irradiance at the planar detector array, we multiplied by the conical solid angle Ω = 0.15π sr — accounting for the aperture-limited detector field-of-view of θ = 45°. Then we estimated the change in irradiance with respect to temperature ($dE_{e,\mathrm{bb}}/dT$) near T = 297 K. The detector irradiance noise was compared to the irradiance from a single comb tooth of index m, $E_{e,m} = P_m/A_m$, where P_m = 10 nW is the estimated optical power per comb tooth and A_m = 2300 µm^2 is the estimated area covered by a resolved comb tooth of imaged radius r = 27 µm (equivalent to 1.8 pixels):

$$(\mathrm{SNR})_{\mathrm{d}} = E_{e,m} / \left(\frac{dE_{e,\mathrm{bb}}}{dT}\mathrm{NETD}\right) \approx 2100. \qquad (2)$$

The photon shot-noise-limited SNR is estimated from the square-root of the maximum time-integrated number of photoelectrons per pixel. First, we estimate the maximum number of time-integrated photons per pixel as

$$N_{\mathrm{photons}} = P_m \Delta t G^p(0)/(h\nu), \qquad (3)$$

where Δt is the camera integration time, $G^p(0)$ is the maximum of the area-normalized ILS function in units of pixel^{-1}, h is the Planck constant, $\nu = c/\lambda$ is the photon frequency, c is the speed of light. Then, for Δt = 100 µs, $G^p(0)$ = 0.23 pixel^{-1}, λ = 1.56 µm and a InSb detector quantum efficiency of η_{QE} = 0.95:

$$(\mathrm{SNR})_{\mathrm{s}} = \sqrt{\eta_{\mathrm{QE}} N_{\mathrm{photons}}} \approx 1300. \qquad (4)$$

Finally, the quantization-noise-limited SNR due to finite camera bit depth of n = 14 bits is estimated from the quantity $\eta_{QE}N_{photons}$ divided by the charge capacity of each pixel, N_{e-} = 6.5 × 10^6 multiplied by the maximum number of digitizer counts, $C_{max} = 2^n$ = 16 384:

$$(\mathrm{SNR})_q = \frac{\eta_{QE}N_{photons}}{N_{e-}} C_{max} \approx 4300. \qquad (5)$$

From the quadrature sum of noise levels, we anticipate an achievable single-image SNR ≈ 1100 for P_m = 10 nW. The SNR on a transmission spectrum calculated from the ratio of two such images would then be SNR = 1100/$\sqrt{2}$ ≈ 780, resulting in a transmission spectrum baseline noise of 1/SNR = 0.0013.

Results and discussion

The $2\nu_1$ band of $H^{13}CN$ near λ = 1.56 μm

The direct frequency comb spectrum of the $H^{13}CN$ recorded over a wavelength (wavenumber) range of λ = 1.548 μm to λ = 1.565 μm ($\tilde{\nu}$ = 6388 cm^{-1} to $\tilde{\nu}$ = 6458 cm^{-1}) is plotted in the top panel of **Fig. 5**. The transmission spectrum — recorded in 200 μs per grating position, over a total of six positions — is plotted as blue dots. The HITRAN2020 simulation is plotted as the red line and inverted for clarity.

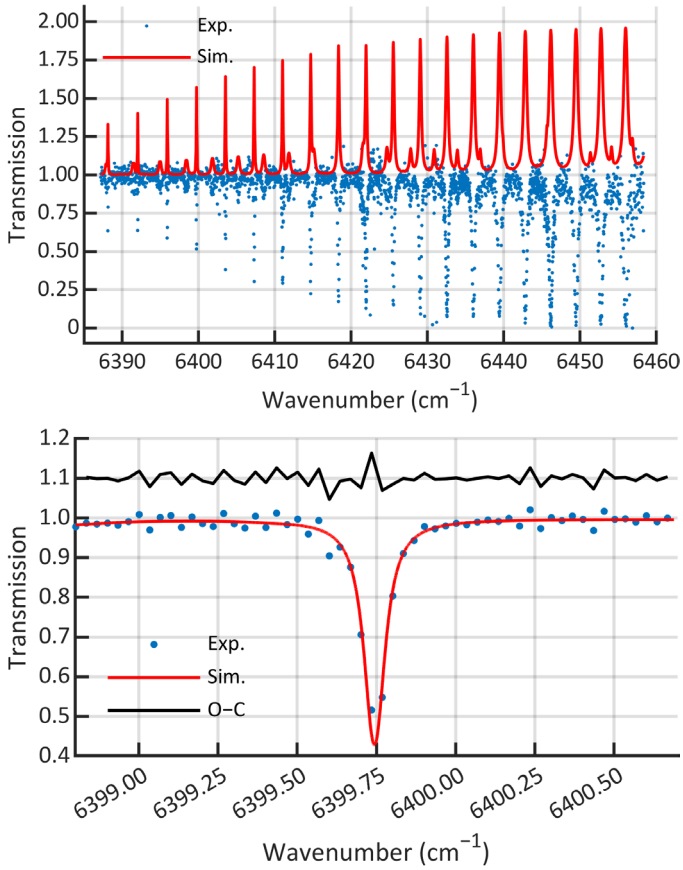

Fig. 5. Direct frequency comb spectroscopy of the $2\nu_1$ band of $H^{13}CN$ near λ = 1.56 μm. Top panel, comb-tooth-resolved transmission spectrum of $H^{13}CN$ (Exp., blue dots) and HITRAN2020 simulation (inverted; Sim., red line). Bottom panel, a zoom-in near the P 25e transition at 6399.744 cm^{-1}. There, the standard deviation of the observed-minus-calculated residuals (offset by +1.1; O–C, black line) is 0.017.

At each grating position, the experimental transmission spectrum was calculated from the ratio of two images, obtained by alternating the 1×2 fiber optic switch between sample and reference paths. Each image was background-subtracted using a blank camera image (no comb light) recorded before or after the probe and reference image series, and normalized counts from each column were fitted to a 3rd-order polynomial baseline function along with the HITRAN2020 model simulated at experimental conditions using Voigt line profiles.

The observed SNR for the data in **Fig. 5** is below the projections reported earlier in the paper. One source of reduced SNR is the optical transmission through the sample arm of the fiber-optic switch illustrated in **Fig. 2**. The comb-tooth counts in the sample probe images are a factor 30 lower than in the reference image — a result of broadband optical attenuation likely due to a malfunctioning or damaged fiber component. Reducing the power per comb mode from P_m = 10 nW to P_m = 0.33 nW reduces the expect detector-noise-limit to SNR ≈ 71 — or a baseline noise level of 1/SNR = 0.014.

This lower SNR predicted at the observed lower optical power is commensurate with the standard deviation of the fitted residuals found for the P 25e transition of the $2\nu_1$ band of $H^{13}CN$. The observed-minus-calculated residuals are plotted in the bottom panel of **Fig. 5** as a black line, offset for clarity by +1.1. The standard deviation of the residuals from a Voigt line profile is 0.017, for a maximum spectral SNR ≈ 58. Progress towards closing this SNR gap for the two-image transmission spectrum is ongoing. The results will improve our ability to test various HCN line lists against precision direct frequency comb spectroscopy.

Outlook

Mid-infrared direct frequency comb spectroscopy

In addition to the short-wave infrared direct frequency comb spectroscopy of $H^{13}CN$ reported here, we also introduce our instrumentation for precision mid-wave infrared spectroscopy in the vicinity of the $3\nu_2$ band of $H^{12}CN$ near λ = 4.73 μm (2115 cm^{-1}).

The laser source for our mid-wave infrared system is a commercial difference frequency generation comb (Menlo Systems; Mid-IR Comb) with tuneable output from 4.45 μm to 4.75 μm and instantaneous bandwidth of >90 cm^{-1}. The comb has a repetition rate of f_{rep} = 0.250 GHz and a carrier envelope offset frequency equal to zero by design [33]. The cross-dispersed spectrometer comprises a VIPA etalon (Light Machinery; OP-7553-3000-1), ruled diffraction grating and camera, and performs over a bandwidth of 30 cm^{-1} per grating position as previously demonstrated on N_2O [31].

Beyond quantitative line-by-line analysis of rotationally resolved vibrational spectra, cross-dispersed spectrometers can also be leveraged to study broadly absorbing species. Shown in **Fig. 6** is an experimental transmission spectrum for a pure sample of sulfur hexafluoride (SF_6) recorded at a pressure of 99.8 kPa and a temperature of 297 K (blue line) compared

to reference data from the Pacific Northwest National Laboratory (PNNL) gas-phase spectral database (red line, inverted) [34]. PNNL absorbance data was converted to spectral transmittance [35,36] and then convolved with the median value for the empirically derived ILS function from contemporary experiments on N_2O reported in Bailey et al. [31]. The sample path length was 7 cm.

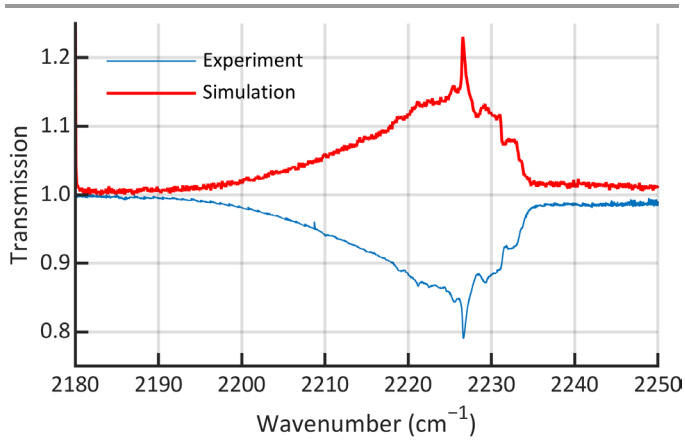

Fig. 6. Direct frequency comb spectrum of SF_6 (Experiment, blue line) recorded in the mid-wave infrared at a wavelength near 4.49 µm. Also plotted is the spectrum from the PNNL database (inverted; Simulation, red line) [34], convolved with our estimated instrument line shape (ILS) function [31].

The spectrum of SF_6 is reported here as a test case for our mid-infrared system. The results illustrate potential for quantitative evaluation of a range of molecular targets including complex organic molecules like polycyclic aromatic hydrocarbons (PAHs) and simple alcohols (i.e., methanol) — many of which are useful to probe astrochemical and astrophysical phenomena [37].

Conclusions

Presented here is an experimental setup to perform direct frequency comb spectroscopy of $H^{13}CN$ in the short-wave infrared near a wavelength of 1.56 µm. We used a mode-locked laser with repetition rate of 1.00 GHz as the laser source and a cross-dispersed design with a virtually imaged phased array as the spectrometer. The studied ^{13}C-enriched HCN gas sample was contained within a commercial glass-sealed and fiber-coupled optical multipass cell. We report an initial spectrum of $H^{13}CN$ in the short-wave infrared and compare with a model from HITRAN2020. The initial results show good agreement with the database, but at reduced experimental signal-to-noise ratio due to optical power losses upstream of the spectrometer.

Future work will focus on applying this experimental setup to measure high-precision and low-uncertainty spectral reference data including parameters like intensities, positions and line-shapes. We also aim to compare our results with those obtained from dual electro-optic frequency comb spectroscopy (e.g., [16]), and to apply our cross-dispersed spectrometer approach to the direct frequency comb spectroscopy of $H^{12}CN$ in the mid-wave infrared near a wavelength of 4.73 µm.

Author contributions

D. Michelle Bailey: Investigation, Formal analysis, Methodology, Software, Visualization, Writing – reviewing and editing. **Eric M. Crump:** Validation, Visualization, Writing – reviewing & editing. **Joseph T. Hodges:** Formal analysis, Methodology, Supervision, Writing – reviewing & editing. **Adam J. Fleisher:** Conceptualization, Investigation, Formal analysis, Data curation, Funding acquisition, Supervision, Visualization, Writing – original draft, Writing – reviewing & editing.

Conflicts of interest

There are no conflicts to declare.

Acknowledgements

We acknowledge Eduardo Oteiza (Vescent Photonics) and Florian Emaury (Menhir Photonics) for loaning the mode-locked laser (MENHIR-1550), Ibrahim Sadiek (Leibniz Institute for Plasma Science and Technology, INP Greifswald, Germany) for discussing comb-mode-resolved spectrometers and Eisen Gross (National Institute of Standards and Technology, NIST) and Jake Connors (NIST) for reading the manuscript. Funding was provided by NIST and we acknowledge an award from the National Aeronautics and Space Administration (NASA) Astrophysics Research and Analysis (APRA) program NH21ZDA001N-APRA.

Notes and references

‡ Certain commercial equipment is identified in this paper to foster understanding. Such identification does not imply recommendation or endorsement by the National Institute of Standards and Technology (NIST), nor does it imply that the equipment identified is necessarily the best available for the purpose.

1 T. Horota, S. Yamamoto, H. Mikami and M. Ohishi, *Astrophys. J.,* 1998, **503,** 717.
2 S. Nickerson, N. Rangwala, S. W. J. Colgan, C. DeWitt, X. Huang, K. Acharyya, M. Drozkovskaya, R. C. Fortenberry, E. Herbst and T. J. Lee*, Astrophys. J.*, 2021, **907,** 51.
3 M. A. Cordiner, M. Y. Palmer, M. de Val-Borro, S. B. Charnley, L. Paganini, G. Villanueva, D. Bockelée-Morvan, N. Biver, A. J. Remijan, Y.-J. Kuan, et al., *Astrophys. J. Lett.* 2019, **870,** L26.
4 M. Rengel, D. Shulyak, P. Hartogh, H. Sagawa, R. Moreno, C. Jarchow and D. Breitschwerdt, *Astron. Astrophys.,* Manuscript no. 41422-vf, arXiv:2112.04125 [astro-ph.EP].
5 E. Lellouch, M. Gurwell, B. Butler, T. Fouchet, P. Lavvas, D. F. Strobel, B. Sicardy, A Moulet, R. Moreno, D. Bockelée-Morvan, et al. *Icarus,* 2017, **286,** 289.
6 A. Tsiaras, M. Rocchetto, I. P. Waldmann, O. Venot, R. Varley, G. Morello, M. Damiano, G. Tinetti, E. J. Barton and S. N. Yurchenko, *Astrophys. J.,* 2016, **820,** 99.

7 P. Giacobbe, M. Brogi, S. Gandhi, P. E. Cubillos, A. S. Bonomo, A. Sozzetti, L. Fossati, G. Guilluy, I. Carleo, M. Rainer, et al., *Nature,* 2021, **592,** 205.
8 V. S. Magalhães, P. Hily-Blant, A. Faure, M. Hernandez-Vera and F. Lique,
9 B. Riaz, W.-F. Thi and P. Caselli, *Mon. Not. Roy. Astron. Soc.,* 2018, **481,** 4662. *Astron. Astrophys.* 2018, **615,** A52.
10 R. J. Barber, J. K. Strange, C. Hill, O. L. Polyansky, G. Ch. Mellau, S. N. Yurchenko and J. Tennyson, *Mon. Not. Roy. Astron. Soc.,* 2014, **437,** 1828.
11 J. Fortney, T. D. Robinson, S. Domagal-Goldman, A. D. Del Genio, I. E. Gordon, E. Gharib-Nezhad, N. Lewis, C. Sousa-Silva, V. Airapetian, D. Drouin, et al., arXiv:1905.07064 [astro-ph.EP].
12 I. E. Gordon, L. S. Rothman, R. J. Hargreaves, R. Hashemi, E. V. Karlovets, F. M. Skinner, E. K. Conway, C. Hill, R. V. Kochanov, Y. Tan, et al. *J. Quant. Spectrosc. Radiat. Transfer,* 2022, **277,** 107949.
13 T. Delahaye, R. Armante, N. A. Scott, N. Jacquinet-Husson, A. Chédin, L. Crépeau, C. Crevoisier, V. Douet, A. Perrin, A. Barbe, et al., *J. Mol. Spectrosc.,* 2021, **380,** 111510.
14 J. Tennyson, S. N. Yurchenko, A. F. Al-Refaie, V. H. J. Clark, K. L. Chubb, E. K. Conway, A. Dewan, M. N. Gorman, C. Hill, A. E. Lynas-Gray, et al., *J. Quant. Spectrosc. Radiat. Transfer,* 2020, **255,** 107228.
15 V. Yu. Makhnev, A. A. Kyuberis, O. L. Polyansky, I. I. Mizus, J. Tennyson and N. F. Zobov, *J Mol. Spectrosc.,* 2019, **353,** 40.
16 P. Guay, J. Genest and A. J. Fleisher, *Opt. Lett.,* 2018, **43,** 1407.
17 G. Ch. Mellau, V. Yu. Makhnev, I. E. Gordon, N. F. Zobov, J. Tennyson and O. L. Polyansky, *J. Quant. Spectrosc. Radiat. Transfer,* 2021, **270,** 107666.
18 J. L. Hall, *Rev. Mod. Phys.,* 2006, **78,** 1279.
19 T. W. Hänsch, *Rev. Mod. Phys.,* 2006, **78,** 1297.
20 A. Foltynowicz, P. Masłowski, T. Ban, F. Adler, K. C. Cossel, T. C. Briles and J. Ye, *Faraday Discuss.,* 2011, **150,** 23.
21 N. Picqué and T. W. Hänsch, *Nat. Photon.,* 2019, **13,** 146.
22 T. Fortier and E. Baumann, *Commun. Phys.,* 2019, **2,** 153.
23 D. M. B. Lesko, A. J. Lind, N. Hoghooghi, A. Kowligy, H. Timmers, P. Sekhar, B. Rudin, F. Emaury, G. B. Rieker and S. Diddams, *OSA Continuum,* 2020, **3,** 2070.
24 S. A. Diddams, L. Hollberg and V. Mbele, *Nature,* 2007, **445,** 627.
25 L. Nugent-Glandorf, T. Neely, F. Adler, A. J. Fleisher, K. C. Cossel, B. Bjork, T. Dinneen, J. Ye and S. A. Diddams, *Opt. Lett.,* 2012, **37,** 3285.
26 G. Kowzan, K. F. Lee, M. Paradowska, M. Borkowski, P. Ablewski, S. Wójtewicz, K. Stec, D. Lisak, M. E. Fermann, R. S. Trawiński and P. Masłowski, *Opt. Lett.,* 2016, 41, 974.
27 F. Karim, S. K. Scholten, C. Perrella and A. N. Luiten, *Phys. Rev. Appl.,* 2020, **14,** 024087.
28 F. C. Roberts, H. J. Lewandowski, B. F. Hobson and J. H. Lehman, *Mol. Phys.,* 2020, **118,** e1733116.
29 I. Sadiek, N. Lang and J. H. van Helden, "An Air-spaced Virtually Imaged Phased Array Spectrometer Based on a Mid-Infrared Optical Frequency Comb," in *Optical Sensors and Sensing Congress 2022 (AIS, LACSEA, Sensors, ES),* Technical Digest Series (Optica Publishing Group), paper LM4B.5.
30 S. Xiao, A. M. Weiner and C. Lin, *IEEE J. Quantum Electron.,* 2004, **40,** 420.
31 D. M. Bailey, G. Zhao and A. J. Fleisher, *Anal. Chem.,* 2020, **92,** 13759.
32 www.spectralcalc.com/blackbody_calculator; accessed 24 January 2023.
33 M. Zimmermann, C. Gohle, R. Holzwarth, T. Udem and T. W. Hänsch, *Opt. Lett.,* 2004, **29,** 310.
34 S. W. Sharpe, T. J. Johnson, R. L. Sams, P. M. Chu, G. C. Rhoderick and P. A. Johnson, *Appl. Spectrosc.,* 2004, **58,** 1452.
35 J. J. Harrison and P. F. Bernath, *J. Quant. Spectrosc. Radiat. Transfer,* 2010, **111,** 1282.
36 H. Yi and A. J. Fleisher, *J. Chem. Phys.,* 2019, **151,** 234202.
37 K. I. Öberg, *Chem. Rev.* 2016, **116,** 9631.